Strathprints Institutional Repository

Corson, Lindsey T. (2011) Maximizing the heat flux in steady unicellular porous media convection. In: 2011 Summer Program in Geophysical Fluid Dynamics. Woods Hole Oceanographic Institution, Woods Hole, Massachusetts, pp. 389-412. ,

This version is available at http://strathprints.strath.ac.uk/50943/

Maximizing the heat flux in steady unicellular porous media convection

Lindsey T. Corson
University of Strathclyde

1   Introduction

Convection in a horizontal porous layer heated from below is relevant to a variety of geological and engineering applications (Nield & Bejan [13]; Phillips [16], [17]). Porous media convection has been studied extensively, beginning with the linear stability analyses of Horton and Rogers [9] and Lapwood [11], and the flow dynamics and bifurcation structure for low to intermediate Rayleigh numbers (Ra) have been thoroughly explored both theoretically and numerically (Graham and Steen [7]). Asymptotic descriptions of steady porous media convection have been proposed by Palm *et al.* [15], Robinson & O'Sullivan [18], and Rudraiah & Musuoka [19], although there is a distinct lack of agreement among these and other authors regarding the asymptotic form of the convection.

It has been firmly established that the classical marginally stable boundary layer argument of Howard [10] for Rayleigh-Bénard convection at high Rayleigh number also holds for porous media convection (Horne & O'Sullivan [8]). This argument gives a scaling $Nu \sim Ra$, where the Nusselt number, Nu, represents the heat transport; a result supported by rigorous upper bound theory (Doering & Constantin [5]). However, Graham and Steen [7] note that this scaling is only valid after the onset of plumes, at approximately $Ra = 700$; for smaller Ra the appropriate scaling is $Nu \sim Ra^{2/3}$ (Cherkaoui & Wilcock [3]).

The high resolution two-dimensional (2D) direct numerical simulations (DNS) of Otero *et al.* [14] in a horizontally periodic layer indicate that as the Rayleigh number is increased, the heat transport shifts from being described by the classical $Nu \sim Ra$ scaling to being better described by $Nu \sim Ra^{0.9}$. Crucially, their simulations show that the spacing between the thermal plumes decreases as Ra is increased. From the data presented, it appears that the inter-plume spacing may scale in direct proportion to the wavelength of the fastest growing linear mode ($\sim Ra^{-1/4}$). The experimental results of Lister [12], by contrast, suggest the inter-plume spacing scales as $(Ra + C)^{-1/2}$, for some constant C.

Motivated in part by these prior investigations, the primary aim of the present study is to determine the maximum heat transport attainable in steady 2D unicel-

lular porous media convection. By focusing on this restricted class of flows we are able to use an efficient iterative numerical scheme to systematically probe the way in which the heat transport depends on the inter-plume spacing. Guided by our numerical results, we also propose a large-Ra asymptotic reduction of the governing equations that yields the asymptotic structure of the solutions giving the maximum heat transport.

The remainder of this report is organised as follows. In §2 we formulate the standard mathematical model of porous media convection and recall the key results of linear stability theory for this system. The numerical method used to find (generally unstable) steady-state high-Ra solutions is described in §3 along with a synopsis of our numerical results. In §4 we propose a multi-region matched asymptotic description of the maximal Nusselt number solutions, motivated by the numerical solutions described in §3. In §5 we use our steady-state solutions as initial conditions in a time-dependent numerical model and analyse the results. Finally, in §6 we summarise our findings and outline avenues for future work.

2 Problem formulation

We consider a fluid-saturated porous layer heated from below at $z = 0$ and cooled from above at $z = 1$. The evolution of the 2D velocity $\mathbf{u}(\mathbf{x}, t) = (u, w)$, temperature $T(\mathbf{x}, t)$ and pressure $p(\mathbf{x}, t)$ fields is governed by the non-dimensional Darcy-Oberbeck-Boussinesq equations (Nield & Bejan [13]) in the infinite Darcy–Prandtl number limit. In streamfunction–vorticity form, these equations can be expressed as

$$\nabla^2 \psi = -Ra \frac{\partial T}{\partial x}, \tag{1}$$

$$\frac{\partial T}{\partial t} + \frac{\partial \psi}{\partial z} \frac{\partial T}{\partial x} - \frac{\partial \psi}{\partial x} \frac{\partial T}{\partial z} = \nabla^2 T. \tag{2}$$

Here ψ is the streamfunction describing cellular flow in the (x, z)–plane. The dimensionless parameter $Ra = KHg\beta\Delta T/(\nu\kappa_m)$ is the Rayleigh number, where K is the permeability of the medium, H is the depth of the layer, g is the gravitational acceleration, β is the thermal expansion coefficient, ΔT is the temperature difference across the layer, ν is the kinematic viscosity, and κ_m is the effective diffusivity of heat through the saturated medium.

The non-dimensional temperature at the top and bottom of the layer is held fixed at 0 and 1, respectively, and we seek steady unicellular solutions with discrete translational invariance in the horizontal coordinate x and reflection symmetry about the planes $x = n\pi/k$ for integer n and given cell width $L = \pi/k$, where k is the horizontal wavenumber. Since we are interested in unicellular convection we will take $n = 1$ throughout. Therefore, we impose the following boundary and symmetry conditions:

$$T(x,0,t) = 1, \quad T(x,1,t) = 0, \quad \psi(x,0,t) = 0, \quad \psi(x,1,t) = 0,$$
$$\frac{\partial T}{\partial x}(0,z,t) = 0, \quad \frac{\partial T}{\partial x}(L,z,t) = 0, \quad \psi(0,z,t) = 0, \quad \psi(L,z,t) = 0. \tag{3}$$

It is useful to recapitulate a few results from linear stability theory (Nield & Bejan [13], Chapter 6). If we define $T = (1 - z) + \tilde{\theta}(x,z,t)$, where $1 - z$ is the conduction solution, and search for solutions of the linearised versions of (1) and (2) of the form

$$\tilde{\theta}(x,z,t) = \cos(kx)\sin(\pi z)e^{\sigma t}, \quad \psi(x,z,t) = \Psi\sin(kx)\sin(\pi z)e^{\sigma t}, \tag{4}$$

we find that the (strictly real) growth rate σ is given by

$$\sigma = \frac{Ra}{k^2 + \pi^2} - (k^2 + \pi^2). \tag{5}$$

From this relationship, it is easily shown that the critical wavenumber $k^{\text{crit}} = \pi$, implying the critical cell width $L^{\text{crit}} = 1$ and that the critical Rayleigh number $Ra^{\text{crit}} = 4\pi^2$. Moreover, for large Rayleigh number, the wavenumber k_f of the fastest growing linear mode is given by

$$k_f \sim \sqrt{\pi} Ra^{1/4}. \tag{6}$$

A useful quantity in the study of convection is the normalised volume-averaged vertical heat flux, or Nusselt number,

$$Nu = 1 + \frac{1}{L}\left\langle \int \frac{\partial \psi}{\partial x} T \mathrm{d}x\mathrm{d}z \right\rangle, \tag{7}$$

where the angle brackets indicate the long-time average

$$\langle f \rangle = \lim_{T \to \infty} \frac{1}{T} \int_0^T f(t)\mathrm{d}t. \tag{8}$$

From the equations of motion we can derive an equivalent expression for the Nusselt number,

$$Nu = -\frac{1}{L}\left\langle \int_{z=0} \frac{\partial T}{\partial z}\mathrm{d}x \right\rangle. \tag{9}$$

This expression shows that Nu can also be interpreted as the ratio of the horizontally-integrated, time-averaged vertical heat flux to the corresponding value realized in the absence of convection.

3 Numerical simulations

We compute time-independent numerical solutions of (1)–(2), subject to the boundary conditions (3), using a Newton–Kantorovich iteration scheme (Boyd [2], Appendix C). We begin by rewriting the model equations as

$$\nabla^2 \psi = F^\psi(T_x), \tag{10}$$

$$\nabla^2 T = F^T(\psi_x, \psi_z, T_x, T_z), \tag{11}$$

where a subscript denotes a partial derivative with respect to the given variable. Suppose we have iterates $T^{(i)}(x,z)$ and $\psi^{(i)}(x,z)$, which are good approximations to the true solutions $T(x,z)$ and $\psi(x,z)$. Taylor expanding the functions F^ψ and F^T in (10) and (11) about the ith iterate gives

$$\nabla^2 \psi = F^\psi(T_x^{(i)}) + F_{T_x}^\psi(T_x^{(i)})[T_x - T_x^{(i)}] + \mathcal{O}\left([T_x - T_x^{(i)}]^2\right) \tag{12}$$

$$\begin{aligned}
\nabla^2 T = & F^T(\psi_x^{(i)}, \psi_z^{(i)}, T_x^{(i)}, T_z^{(i)}) + F_{\psi_x}^T(\psi_x^{(i)}, \psi_z^{(i)}, T_x^{(i)}, T_z^{(i)})[\psi_x - \psi_x^{(i)}] \\
& + F_{\psi_z}^T(\psi_x^{(i)}, \psi_z^{(i)}, T_x^{(i)}, T_z^{(i)})[\psi_z - \psi_z^{(i)}] + F_{T_x}^T(\psi_x^{(i)}, \psi_z^{(i)}, T_x^{(i)}, T_z^{(i)})[T_x - T_x^{(i)}] \\
& + F_{T_z}^T(\psi_x^{(i)}, \psi_z^{(i)}, T_x^{(i)}, T_z^{(i)})[T_z - T_z^{(i)}] \\
& + \mathcal{O}\left([\psi_x - \psi_x^{(i)}]^2, [\psi_z - \psi_z^{(i)}]^2, [T_x - T_x^{(i)}]^2, [T_z - T_z^{(i)}]^2\right),
\end{aligned} \tag{13}$$

where, for example, $F_{T_x}^T$ denotes the Frechet derivative of the function $F^T(\psi_x, \psi_z, T_x, T_z)$ with respect to T_x. By defining correction terms

$$\psi^{(i+1)} \equiv \psi^{(i)} + \hat{\phi}, \quad T^{(i+1)} \equiv T^{(i)} + \hat{\theta}, \tag{14}$$

and computing the Frechet derivatives, the linear differential equations for the corrections are given by

$$\nabla^2 \hat{\phi} + Ra\hat{\theta}_x = F^\psi(T_x^{(i)}) - \nabla^2 \psi^{(i)}, \tag{15}$$

$$\nabla^2 \hat{\theta} + T_z^{(i)} \hat{\phi}_x - T_x^{(i)} \hat{\phi}_z - \psi_z^{(i)} \hat{\theta}_x + \psi_x^{(i)} \hat{\theta}_z = F^T(\psi_x^{(i)}, \psi_z^{(i)}, T_x^{(i)}, T_z^{(i)}) - \nabla^2 T^{(i)}, \tag{16}$$

subject to the boundary conditions

$$T = 1, \quad \psi = 0, \quad \hat{\theta} = 0, \quad \hat{\phi} = 0 \quad \text{on} \quad z = 0, \tag{17}$$

$$T = 0, \quad \psi = 0, \quad \hat{\theta} = 0, \quad \hat{\phi} = 0 \quad \text{on} \quad z = 1, \tag{18}$$

$$T_x = 0, \quad \psi = 0, \quad \hat{\theta}_x = 0, \quad \hat{\phi} = 0 \quad \text{on} \quad x = 0, \tag{19}$$

$$T_x = 0, \quad \psi = 0, \quad \hat{\theta}_x = 0, \quad \hat{\phi} = 0 \quad \text{on} \quad x = L. \tag{20}$$

Equations (15) and (16) can be rewritten in matrix form

$$\begin{bmatrix} D_{xx} + D_{zz} & RaD_x \\ T_z^{(i)} D_x - T_x^{(i)} D_z & D_{xx} + D_{zz} - \psi_z^{(i)} D_x + \psi_x^{(i)} D_z \end{bmatrix} \begin{bmatrix} \hat{\phi} \\ \hat{\theta} \end{bmatrix} = \begin{bmatrix} -RaT_x^{(i)} - \nabla^2 \psi^{(i)} \\ \psi_z^{(i)} T_x^{(i)} - \psi_x^{(i)} T_z^{(i)} - \nabla^2 T^{(i)} \end{bmatrix}, \tag{21}$$
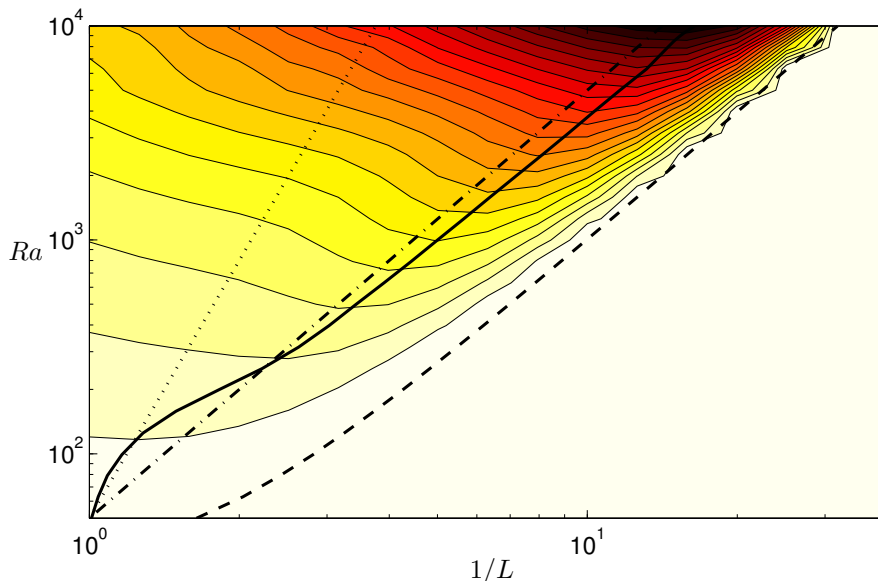
Figure 1: Surface plot of Nusselt number in (Ra, L) parameter space. Darker shading represents higher values of Nu. The solid line marks the ridge along which Nu is maximum; the dashed line is the linear stability boundary; the dashed-dotted line is $L = 50^{1/2}Ra^{-1/2}$; and the dotted line is $L = 50^{1/4}Ra^{-1/4}$. The jagged contours at high Ra are resolution artefacts.

where, for example, D_x denotes the partial derivative with respect to x.

We iterate the system of equations (21) for a given Rayleigh number Ra and cell-width – or inter-plume spacing – L, subject to the boundary conditions (17)–(20), using a pseudospectral collocation method. A convergence criterion requiring $\max(|\hat{\phi}|) < 10^{-10}$ and $\max(|\hat{\theta}|) < 10^{-10}$ was employed. A Chebyshev tensor-product formulation with 60 nodes in both the horizontal and vertical directions was used to provide adequate resolution of the boundary layers.

Simulations were performed starting at $Ra = 50$, just above the critical Rayleigh number $Ra^{\mathrm{crit}} = 4\pi^2 \approx 39.5$, and initial cell width $L = 1$. Once convergence was achieved, Ra was increased by a factor of $10^{1/10}$ with the previous converged state used as the new "initial" condition. This was repeated for cell widths from $L = 1$ to $L = 0.01$, reduced in steps of $10^{1/10}$ in order to thoroughly explore (Ra, L) parameter space. At each point the Nusselt number Nu was recorded.

The results of these simulations are summarized in figures 1 and 2. In figure 1 a surface plot of the Nusselt number in (Ra, L) parameter space is presented. The dashed line indicates the linear stability boundary, $L \sim \pi Ra^{-1/2}$. To the right of this line there is no convection and so $Nu = 1$; the jagged contours at high Ra are resolution artefacts. The solid line denotes the maximum value of Nu, and hence marks a ridge on the surface. To elucidate scalings, the lines $L = 50^{1/2}Ra^{-1/2}$ (dashed–dotted)
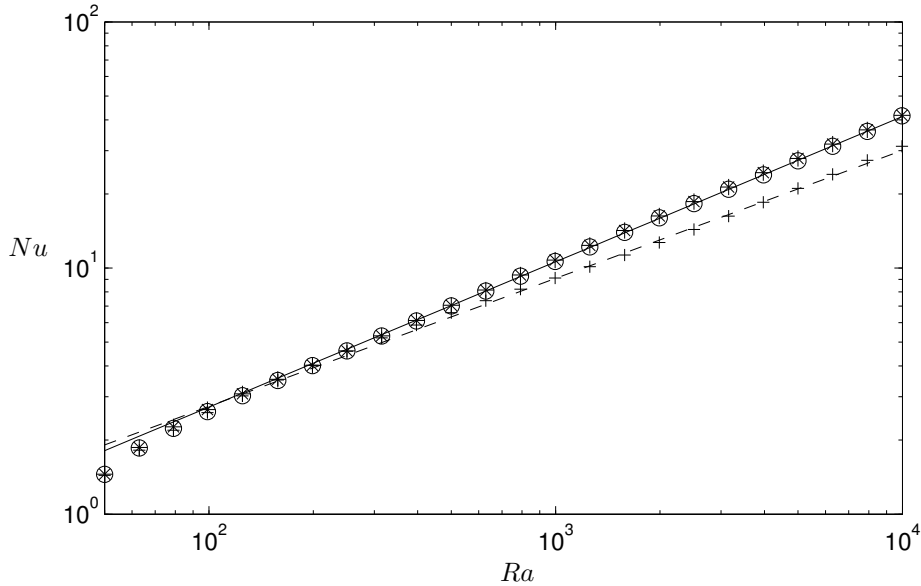
Figure 2: Plot of Nu vs. Ra along different paths $L = L(Ra)$. The asterisks are the data along the maximum Nu ridge; the circles are the data along the curve $L = 50^{1/2}Ra^{-1/2}$, and the crosses are the data along the curve $L = 50^{1/4}Ra^{-1/4}$. The solid line is the best fit curve $0.18Ra^{0.59}$, and the dashed line is the best fit curve $0.25Ra^{0.52}$.

and $L = 50^{1/4}Ra^{-1/4}$ (dotted) are also plotted. The constants $50^{1/2}$ and $50^{1/4}$ were used so that $L = 1$ when $Ra = 50$ in each case.

As noted in § 1, the DNS results presented in Otero *et al.* [14] suggest that the inter-plume spacing scales with the wavelength of the fastest growing linear mode: from (6), $L \sim \pi/k_f = \sqrt{\pi}Ra^{-1/4}$. However, the experimental results of Lister [12] suggest that the inter-plume spacing scales as $(Ra + C)^{-1/2}$. We can see in figure 1 that the maximum Nu ridge satisfies the $L \sim Ra^{-1/4}$ scaling up to $Ra \approx 150$, as it closely follows the dotted line. Above $Ra \approx 150$, the ridge shifts to the right and for $Ra > 500$ it follows the relationship $L \sim 7.02Ra^{-0.52}$. With this scaling, however, the ridge would eventually cross the linear stability boundary into the conduction $Nu = 1$ regime. Therefore, it seems plausible that the maximum Nu ridge (at least for steady 2D unicellular convection) must eventually scale as $L \sim Ra^{-1/2}$, in agreement with Lister's results [12].

Figure 2 shows the variation of Nu with Ra along the ridge (asterisks) and along the curves $L = 50^{1/2}Ra^{-1/2}$ and $L = 50^{1/4}Ra^{-1/4}$ (circles and crosses, respectively). In the range $50 \leq Ra \leq 350$, all three curves lie on top of one another; however, at higher values of Ra the $L = 50^{1/4}Ra^{-1/4}$ curve drops below the other two. Across the range $1000 \lesssim Ra \lesssim 10000$, the data along the curve $L = 50^{1/4}Ra^{-1/4}$ scale as

$Nu \sim 0.25Ra^{0.52}$ (dashed line), and the data along the curve $L = 50^{1/2}Ra^{-1/2}$, as well as the ridge, scale as $Nu \sim 0.18Ra^{0.59}$ (solid line). Although none of these steady-state unicellular solutions exhibits the Nu–Ra scaling presented in Otero *et al.* [14], they do reveal a clear and non-trivial dependence of the heat transport on the inter-plume spacing.

3.1 Solution structure

In this section, we examine the spatial structure of the numerical solutions across the range $1000 \lesssim Ra \lesssim 10000$, where we obtain the clean $Nu \sim Ra^{0.6}$ relationship with a cell width that scales as $L \sim 50^{1/2}Ra^{-1/2}$, to gain further insight into the steady unicellular flows that maximize the heat transport.

Figure 3 shows contour plots of the temperature $T(x, z)$ and streamfunction $\psi(x, z)$ for $Ra = 997$ and $Ra = 9976$. Note the aspect ratio distortion in each set of plots: when $Ra = 997$, $L \approx 0.2239$, and when $Ra = 9976$, $L \approx 0.0708$. Clear evidence of a thermal boundary layer, which thins as Ra is increased, can be seen in figure 3(a) and (c). In figure 3(b) and (d) there is evidence of a momentum boundary layer that also thins as Ra is increased but remains thicker than the thermal boundary layer. Furthermore, in the centre of the cell, which we will denote the core, the streamlines become vertical as Ra increases, suggesting ψ becomes independent of z there.

To extract scalings from the numerical results, it is convenient to decompose the total temperature into its horizontal mean, denoted with an overbar, and a fluctuation; i.e., $T(x, z) = \overline{T}(z) + \theta(x, z)$, where $\theta(x, z)$ is the fluctuation. We note that with this decomposition, (1) and (2) become

$$\nabla^2 \psi = -Ra\frac{\partial \theta}{\partial x}, \tag{22}$$

$$-\frac{\partial}{\partial z}\left(\overline{\frac{\partial \psi}{\partial x}\theta}\right) = \frac{\partial^2 \overline{T}}{\partial z^2}, \tag{23}$$

$$\frac{\partial \psi}{\partial z}\frac{\partial \theta}{\partial x} - \frac{\partial \psi}{\partial x}\frac{\partial \theta}{\partial z} - \frac{\partial \psi}{\partial x}\frac{\partial \overline{T}}{\partial z} + \frac{\partial}{\partial z}\left(\overline{\frac{\partial \psi}{\partial x}\theta}\right) = \nabla^2\theta, \tag{24}$$

where an overbar again denotes a horizontal average.

Figure 4 shows vertical profiles of $\overline{T}$, θ and ψ for $Ra = 9976$. The existence of two distinct boundary layers is now very clear, with the momentum boundary layer being thicker than the thermal boundary layer. In the core, both the temperature fluctuation θ and the streamfunction ψ are independent of z, whereas the average temperature gradient is weakly unstable.

Figure 5 shows horizontal profiles of θ and ψ in both the core (top row) and the thermal boundary layer (bottom row). In the core, the solution appears to consist of a single Fourier mode, whereas in the boundary layer the solution clearly involves a superposition of many Fourier modes.
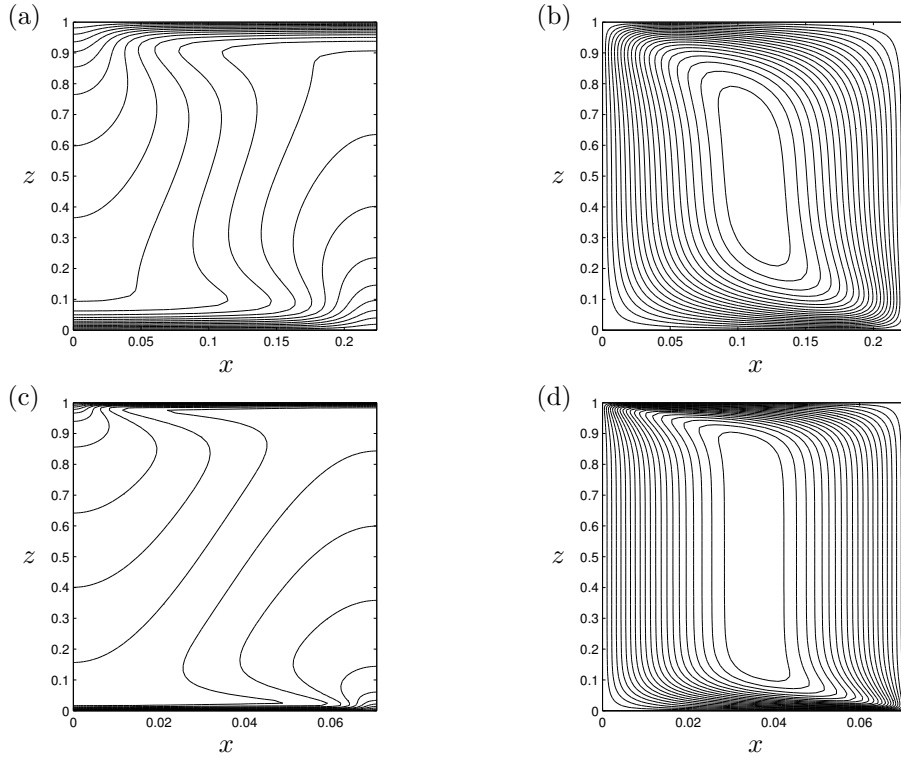
7

Figure 3: Contour plots of (a) temperature $T(x, z)$, (b) streamfunction $\psi(x, z)$ for $Ra = 997$; and (c) temperature $T(x, z)$, (d) streamfunction $\psi(x, z)$ for $Ra = 9976$. In each plot contours are evenly spaced. Note the aspect ratio distortion.
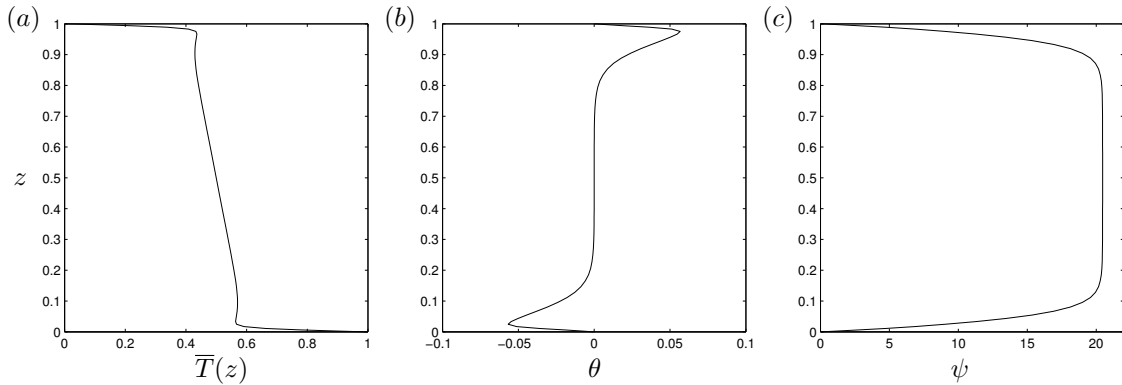

Figure 4: Vertical profiles of (a) $\overline{T}(z)$ and (b) θ and (c) ψ at $x = L/2$ for $Ra = 9976$.

Using these numerical results, we can attempt to quantify the dependencies on Ra of the boundary layer thicknesses and the amplitudes of θ and ψ in the core (figure 6). Since neither boundary layer is uniformly thick across the domain, we plot both the maximum (crosses) and minimum (asterisks) thicknesses of each layer. Figure 6 (a) and (b) shows the results for the thermal and momentum boundary layer, respectively, with the best fit curves for each case shown by the solid and dashed lines.
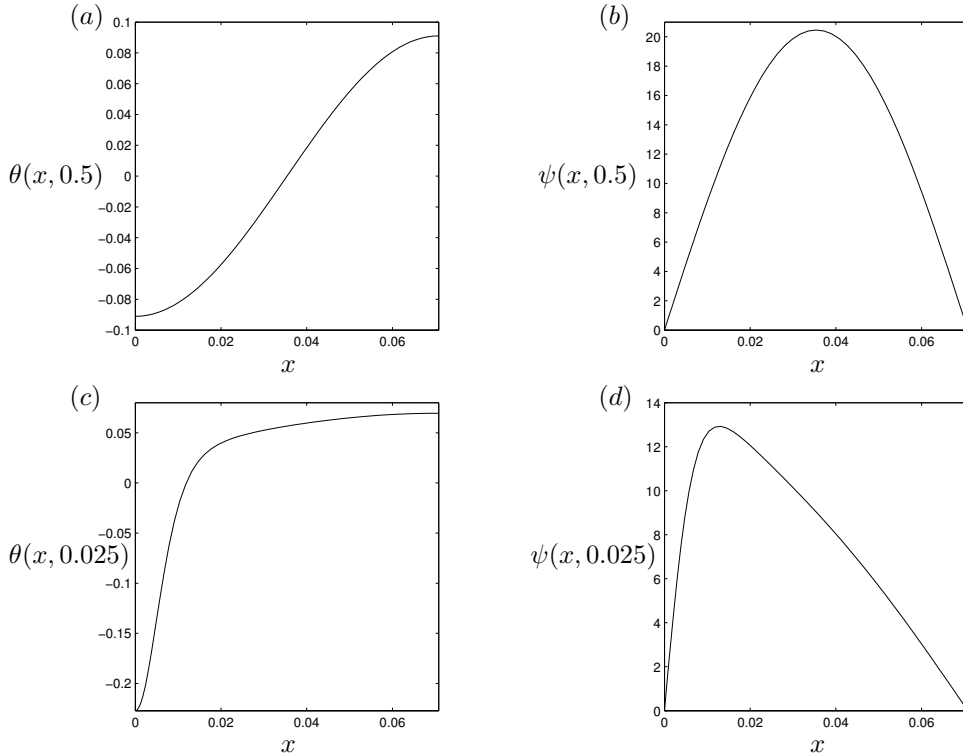
Figure 5: Horizontal profiles of the temperature fluctuation θ (left column) and streamfunction ψ (right column) through the centre of the domain (a, b) and near the bottom of the domain, within the thermal boundary layer (c, d), at $Ra = 9976$.

In the thermal boundary layer both the thickest and thinnest parts of the layer scale as $\delta \sim Ra^{-0.6}$. However, in the momentum boundary layer there is quite a difference between the scalings of the thinnest and thickest parts, with the minimum thickness scaling as $\Delta \sim Ra^{-0.5}$ and the maximum thickness as $\Delta \sim Ra^{-0.2}$.

The amplitude scalings are estimated by plotting the maximum values of θ and ψ in the core region versus Ra, as shown in figure 6 (c) and (d), respectively. The solid line in each plot represents the best fit curve. In this way, we find that in the core $\psi \sim Ra^{0.3}$ and $\theta \sim Ra^{-0.1}$.

4   Asymptotic reduction

Motivated by the numerical results presented in §3, we seek a matched asymptotic description of steady unicellular convection in a cell of varying aspect ratio $L = lRa^{-1/2}$, with $l = \mathcal{O}(1)$, in the large Rayleigh number limit. The numerics suggest that the flow can be divided into three subdomains as shown in figure 7: a core, a momentum boundary layer of thickness Δ, and a thinner thermal boundary layer of thickness δ. This nested boundary layer structure is similar to that presented by Fowler [6] for unicellular porous media convection in a cell of fixed, $\mathcal{O}(1)$ aspect ratio.
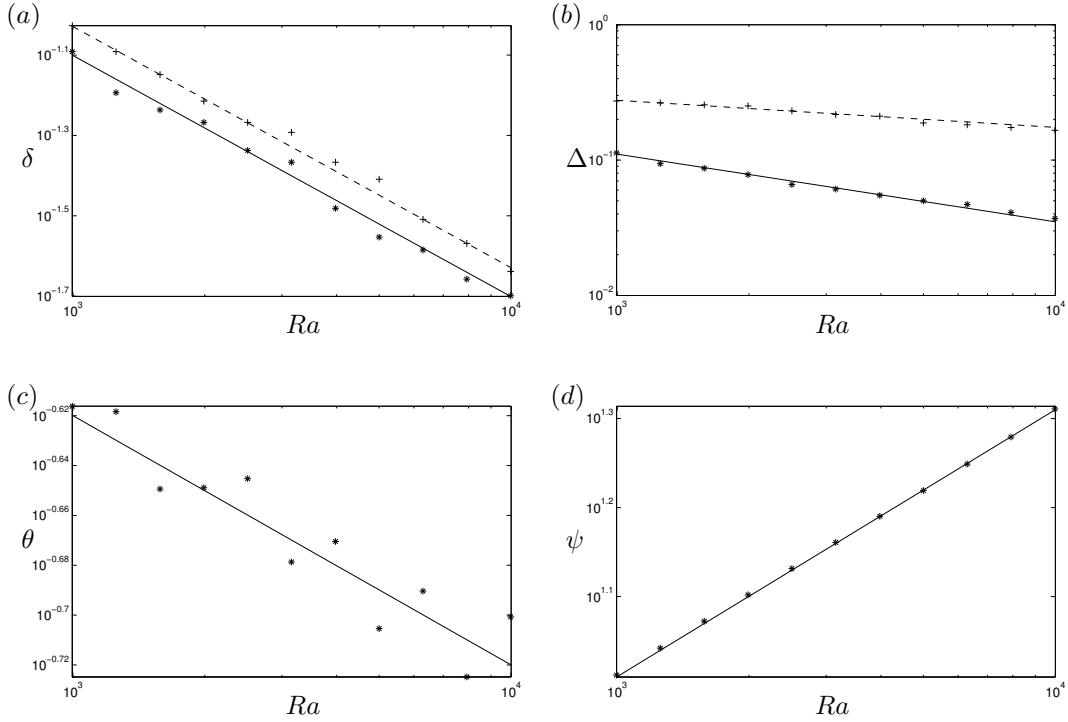
9

Figure 6: (a, b) Approximate location of the minimum (asterisks) and maximum (crosses) thicknesses of the thermal and momentum boundary layers, respectively. The solid lines represent the best fit curve for the minimum thickness: $\delta \sim 5.0Ra^{-0.6}$ for the thermal boundary layer, and $\Delta \sim 3.5Ra^{-0.5}$ for the momentum boundary layer. The dashed lines represent the best fit curve for the maximum thickness: $\delta \sim 5.9Ra^{-0.6}$ for the thermal boundary layer, and $\Delta \sim 1.1Ra^{-0.2}$ for the momentum boundary layer. (c, d) Asterisks represent the approximate maximum values of θ and ψ in the core, respectively. The solid lines in each case indicate the best fit curves $\theta \sim 0.48Ra^{-0.1}$ and $\psi \sim 1.3Ra^{0.3}$.

Each of the subdomains is characterised by a different dominant balance of terms in (22)–(24). The various dominant balances are fixed once the Ra dependencies of the dependent and independent variables in the three subdomains is specified. Here, we opt to determine these scalings *a priori* by insisting that four asymptotic constraints are satisfied and subsequently compare our predictions with the scalings extracted from the numerical results in §3.

Firstly, in the thermal boundary layer, the mean advective and diffusive heat fluxes are both significant. Hence, (23) requires

$$\Psi_B\Theta_B = \frac{1}{\delta Ra^{1/2}}, \tag{25}$$

presuming $\overline{T} = \mathcal{O}(1)$, where Ψ_B and Θ_B are the magnitudes of ψ and θ, at leading order, in the thermal boundary layer. Balancing wall-normal diffusion with advection
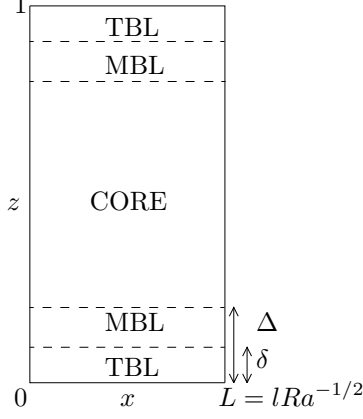
10

Figure 7: Schematic showing hypothesized three-subdomain asymptotic structure for porous media convection at high Rayleigh number.

of the mean temperature in (24) yields

$$\Psi_B = \frac{1}{\delta} Ra^{-1/2} \Theta_B, \tag{26}$$

and combining (25) and (26) then gives

$$\Theta_B = 1, \quad \Psi_B = \frac{1}{\delta Ra^{1/2}}. \tag{27}$$

Secondly, given our hypothesized asymptotic structure, we require ψ_z to vary smoothly everywhere *within* the momentum boundary layer. In particular, this implies

$$\frac{\Psi_M}{\Delta} = \frac{\Psi_B}{\delta}. \tag{28}$$

Thirdly, the existence of the momentum boundary layer requires that z derivatives become comparable to x derivatives in (22), and hence that $\Delta = Ra^{-1/2}$. Equations (26) and (28) then yield

$$\Psi_M = \Psi_B^2 = \frac{1}{\delta^2 Ra}. \tag{29}$$

The final constraint requires the convective heat flux to dominate the diffusive heat flux in the core,

$$-\overline{\psi_x \theta} \sim Q, \tag{30}$$

where Q is the constant advective heat flux there. Since integration of (23) in z gives the exact result

$$-\overline{\psi_x \theta} - \overline{T}_z \equiv Nu, \tag{31}$$

$Q \sim Nu = \mathcal{O}(1/\delta)$, noting that $1/\delta$ is an estimate of the magnitude of $\overline{T}_z$ near $z = 0$ and $z = -1$. Assuming $\Psi_M = \Psi_C$ (see figure 4(c)), then (30) implies

$$\Theta_C = \delta Ra^{1/2}. \tag{32}$$

11

	Numerical	Asymptotic
Nu	$Ra^{0.59}$	$Ra^{2/3}$
δ	$Ra^{-0.6}$	$Ra^{-2/3}$
Δ	$Ra^{-0.2}\text{–}Ra^{-0.5}$	$Ra^{-1/2}$
Θ_C	$Ra^{-0.1}$	$Ra^{-1/6}$
Θ_M	–	$Ra^{-1/6}$
Θ_B	–	1
Ψ_C	$Ra^{0.3}$	$Ra^{1/3}$
Ψ_M	–	$Ra^{1/3}$
Ψ_B	–	$Ra^{1/6}$

Table 1: Comparison of numerical and asymptotic scalings.

Also, in the core, the leading order balance in (22) is

$$\psi_{xx} = -Ra\theta_x. \tag{33}$$

Substituting the scalings for Θ_C and Ψ_C gives $\delta = Ra^{-2/3}$, implying $Nu \sim Ra^{2/3}$.

The complete list of asymptotic scalings is presented in Table 1, along with the numerical scalings found in §3.1 for finite Ra for comparison. Although they do not match identically, there is general agreement between the numerical and asymptotic scalings. Presumably, the discrepancies are attributable either to finite-Ra effects or to inherent limitations in our method of data processing for the numerics.

4.1   Core

In the core, the leading order versions of (22)–(24) are

$$\psi_{C_{xx}} = -Ra\theta_{Cx}, \tag{34}$$
$$-\overline{\psi_{C_x}\theta_C} = Q, \tag{35}$$
$$-\psi_{C_x}\overline{T}_{Cz} = \theta_{Cxx}, \tag{36}$$

where a subscript "C" again refers to a core field. Integrating (34) with respect to x gives

$$\psi_{C_x} = -Ra\theta_C + f(z), \tag{37}$$

where $f(z) = 0$ from mass conservation, and substituting this expression into (35) yields

$$Ra\overline{\theta_C^2} = Q. \tag{38}$$

12

Thus, we deduce that both θ_C and ψ_C are independent of z, in accord with the results of our numerical calculations. Substituting (37) into (36) reveals that the mean temperature gradient within the core must be constant, i.e. $\overline{T}_{Cz} \equiv -g$, say, and that θ_C and hence ψ_C admit single mode solutions:

$$\theta_{Cxx} + Rag\theta_C = 0, \tag{39}$$

and so

$$\theta_C(x) = -\Theta_C \cos(Ra^{1/2}g^{1/2}x). \tag{40}$$

A similar asymptotic structure was found by Blennerhassett & Bassom [1] in their study of strongly nonlinear, high wavenumber Rayleigh–Bénard convection. Because the lateral boundary conditions require $\theta_{Cx} = 0$ at $x = 0, L$, $g = (\pi/l)^2$. In figure 8, this prediction is compared with the exact (numerically computed) mean temperature gradient at $Ra = 9976$ and $l = \sqrt{50}$; the evident excellent agreement provides strong support for the presumed asymptotic structure of the flow within the core. Specifically,

$$\theta_C(x) = -A\Theta_C \cos(Ra^{1/2}\frac{\pi}{l}x), \tag{41}$$

$$\psi_C(x) = \frac{l}{\pi}Ra^{1/2}A\Theta_C \sin(Ra^{1/2}\frac{\pi}{l}x), \tag{42}$$

where $A = \mathcal{O}(1)$ is a constant to be determined, while

$$\overline{T}_C = \frac{1}{2} - \left(\frac{\pi}{l}\right)^2 \left(z - \frac{1}{2}\right). \tag{43}$$

4.2   Momentum boundary layer

In the momentum boundary layer, (22)–(24) become, at leading order,

$$\psi_{Mxx} + \psi_{Mzz} = -Ra\theta_{Mx}, \tag{44}$$

$$-\overline{\psi_{Mx}\theta_{Mz}} = 0, \tag{45}$$

$$\psi_{Mz}\theta_{Mx} - \psi_{Mx}\theta_{Mz} = \psi_{Mx}\overline{T}_{Mz}, \tag{46}$$

presuming $\overline{T}_{Mz} = \mathcal{O}(\Theta_M/\Delta)$ – see figure 4. From (46) it follows that

$$\theta_M = F(\psi_M) - \overline{T}_M(z). \tag{47}$$

Noting that both θ and ψ must smoothly transform from their z-independent profiles in the core to functions of both x and z such that $\theta = F(\psi)$ in the far-field of the momentum boundary layer, we rewrite θ_C as a function of ψ_C:

$$\theta_C(x, z) = F(\psi_C) = \mp A\Theta_C \sqrt{1 - \left(\frac{\pi}{lA\Theta_C}\right)^2 Ra^{-1}\psi_C^2}. \tag{48}$$
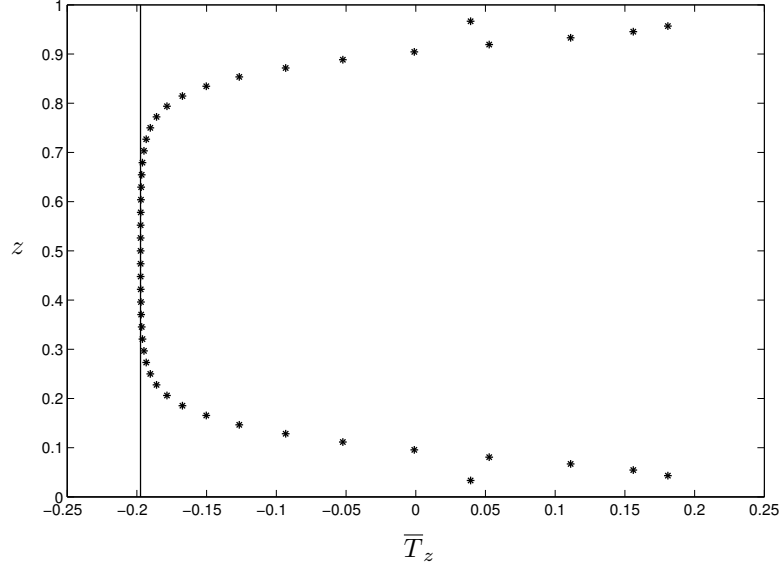
13

Figure 8: Comparison of the numerically computed $\overline{T}_z$ at $Ra = 9976$ and $l = \sqrt{50}$ (asterisks) with the predicted value in the core given by $\overline{T}_{Cz} = (\pi/l)^2$ (solid).

The positive square root applies on the left half of the domain, where $\theta_C < 0$, while the negative square root applies on the right half of the domain, where $\theta_C > 0$. Furthermore, moving from the core to the momentum boundary layer at, say, $z = 0$, $\overline{T}_C \to \overline{T}_M^\infty$, where $\overline{T}_M^\infty$ is the limiting value of $\overline{T}_M(z)$:

$$\overline{T}_M^\infty = \frac{1}{2}\left(1 + \left(\frac{\pi}{l}\right)^2\right). \tag{49}$$

Hence,

$$F(\psi_M) = \mp A\Theta_C\sqrt{1 - \left(\frac{\pi}{lA\Theta_C}\right)^2 Ra^{-1}\psi_M^2} + \overline{T}_M^\infty. \tag{50}$$

Equation (44) becomes a nonlinear Poisson equation for ψ_M:

$$\psi_{Mxx} + \psi_{Mzz} = -RaF'(\psi_M)\psi_{Mx}$$
$$= -\psi_{Mx}\frac{\psi_M}{A\Theta_C}\left(\frac{\pi}{l}\right)^2\left(1 - \left(\frac{\pi}{l}\right)^2\frac{\psi_M^2}{RaA^2\Theta_C^2}\right)^{-1/2}, \tag{51}$$

subject to the boundary conditions

$$\psi_M = 0 \text{ on } x = 0, L \text{ and } z = 0, \text{ and as } Z \equiv \frac{z}{\Delta} \to \infty, \psi_M \to \psi_C. \tag{52}$$

We can then use (47) to find $\theta_M(x, z)$ once $\overline{T}_M(z)$ has been determined, presumably by requiring $\overline{\theta}_M = 0$, in which case $\overline{T}_M(z) = F(\psi_M)$.

14

4.3 Thermal boundary layer

In the thermal boundary layer, the leading order versions of (22)–(24) are

$$\psi_{B_{zz}} = -Ra\theta_{B_x}, \tag{53}$$

$$-\overline{\psi_{B_x}\theta_{B_z}} = \overline{T}_{B_{zz}}, \tag{54}$$

$$\psi_{B_z}\theta_{B_x} - \psi_{B_x}\theta_{B_z} - \psi_{B_x}\overline{T}_{B_z} + \overline{\psi_{B_x}}\theta_{B_z} = \theta_{B_{zz}}. \tag{55}$$

This system is equivalent to

$$\psi_{B_{zz}} = -RaT_{B_x}, \tag{56}$$

$$\psi_{B_z}T_{B_x} - \psi_{B_x}T_{B_z} = T_{B_{zz}}, \tag{57}$$

which must be solved (e.g., at the bottom of the domain) subject to the boundary conditions

$$\psi_B = 0 \text{ on } z = 0,$$
$$T_{B_x} = 0 \text{ on } x = 0, \quad T_B = 1 \text{ on } z = 0, \tag{58}$$
$$\text{and, as } \hat{Z} \equiv \frac{z}{\Delta} \to \infty, \psi_B \to \psi_M \text{ and } T_B \to T_M.$$

5 Time-dependent numerical simulations

Our asymptotic reduction suggests that the heat transport is described by the scaling $Nu \sim Ra^{2/3}$, which differs from the classical scaling $Nu \sim Ra$ of Howard [10] and from that exhibited in the DNS of Otero *et al.* [14]. Therefore, in this section, we employ *time-dependent* simulations to find the heat transport when our steady-state solutions are used as initial conditions.

As before, we consider (1)–(2) subject to the boundary conditions given by (3). Numerical simulations were carried out using a pseudospectral collocation method involving a Chebyshev tensor-product formulation with 70 nodes in both the horizontal and vertical directions to provide adequate resolution of the boundary layers. A semi-implicit time discretization scheme was employed, with the nonlinear and instability terms advanced using a second-order Adams-Bashford method, and the linear diffusive terms advanced using the trapezium rule. The resulting linear algebraic system was solved by direct matrix inversion.

The results of these simulations are summarized in figure 9, which shows the variation of the time-averaged Nu with Ra. In the range $1000 \leq Ra \leq 4000$, the data scale as $Nu \sim Ra^{0.6}$, identically to the steady state scaling found in §3. For $Ra > 4000$, however, the data appear to scale as $Nu \sim Ra^{0.92}$, comparable to the $Nu \sim Ra^{0.9}$ scaling found by Otero *et al.* [14] in a domain of *fixed* width $L = 1$. Of course, the accuracy of this scaling may be suspect given the limited data in this region. Nevertheless, these preliminary results are at least suggestive that Nusselt
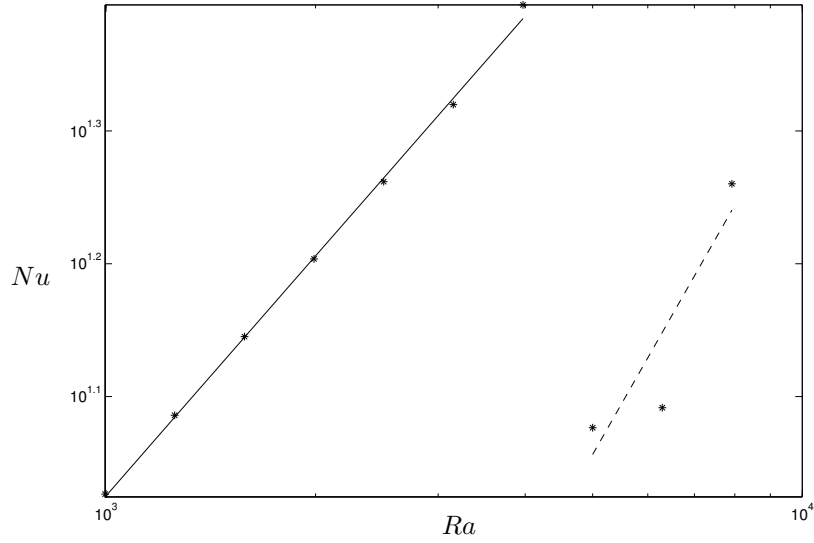
15

Figure 9: Plot of time-averaged Nu against Ra. The solid line is the best fit curve $0.168Ra^{0.6}$, and the dashed line is the best fit curve $0.005Ra^{0.92}$.
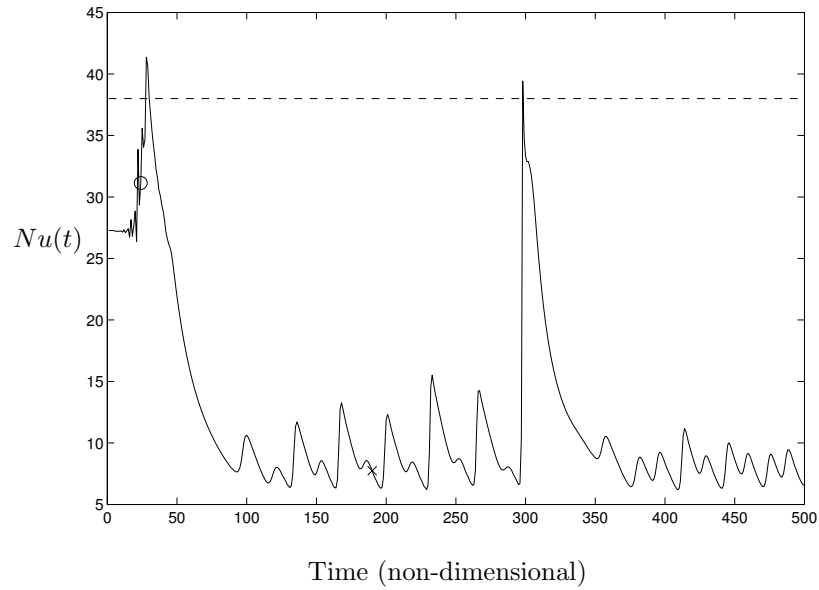

Time (non-dimensional)

Figure 10: Evolution of the Nusselt number for $Ra = 5000$ (solid line). The dashed line represents the approximate value of the long-time average of Nu given by Otero *et al.* [14] at the same Ra in a box of fixed width $L = 1$ (in our notation).
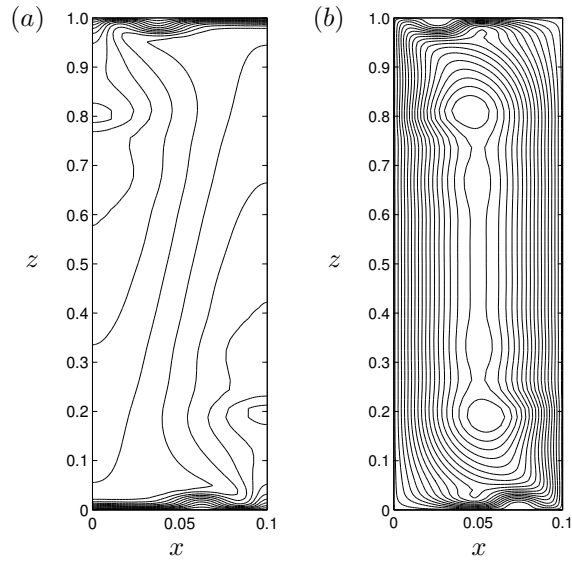
Figure 11: Contour plots of (a) $T(x, z)$, (b) $\psi(x, z)$ for $Ra = 5000$ just before the first peak in $Nu(t)$ (denoted by the circle in figure 10). In each plot contours are evenly spaced. Note the aspect ratio distortion.
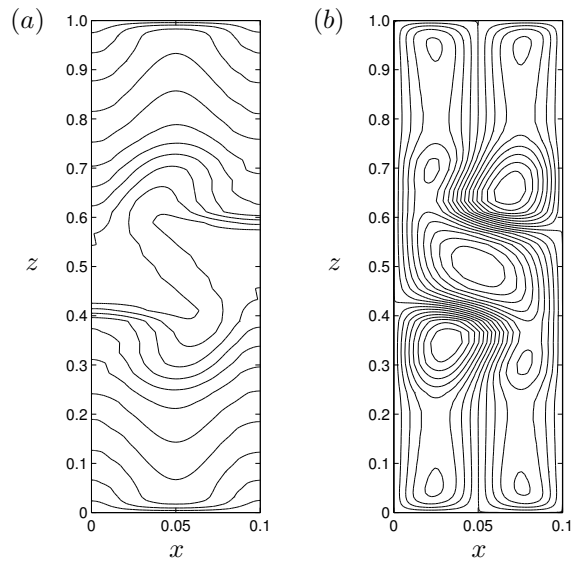

Figure 12: Contour plots of (a) $T(x, z)$, (b) $\psi(x, z)$ for $Ra = 5000$ at a later time (denoted by the cross in figure 10). In each plot contours are evenly spaced. Note the aspect ratio distortion.

17

numbers comparable to those achieved in much wider domains might be attained in narrow domains with aspect ratios shrinking according to $L \sim Ra^{-1/2}$.

Figures 10–12 illustrate the behaviour of the model for $Ra = 5000$, at the start of the $Nu \sim Ra^{0.92}$ regime. Figure 10 shows the evolution of the Nusselt number for $Ra = 5000$, with the dashed line denoting the long-time average value of Nu given by Otero *et al.* [14]. The initial steady solution is unstable, and the time-dependent solution quickly deviates away from it, corresponding with the first increase in $Nu(t)$. The Nusselt number then peaks before settling into a roughly periodic dynamic. Eventually, the system is again excited and the Nusselt number peaks a second time before settling back into a time-periodic behavior.

The temperature and streamfunction fields just before the first peak in the Nusselt number (at the time denoted by the circle in figure 10) are shown in figure 11. In the temperature field (figure 11 (a)) there is evidence of a plume (as defined by Graham & Steen [7]) in the lower (upper) thermal boundary layer at $x \approx 0.06$ ($x \approx 0.04$), corresponding with a roll in the streamfunction field (figure 11 (b)). As noted in §1, Graham & Steen [7] argue that the classical $Nu \sim Ra$ scaling corresponds to the onset of plume formation, which they define to occur when the isotherms contouring the thermal boundary layer become nearly vertical away from the downstream corner of the cell. Furthermore, both DNS and upper bound theory suggest that convection cells within the thermal boundary layer are required to achieve this scaling (Chini *et al.* [4]).

This simulation does not, however, achieve the same overall long-time average value of Nu as Otero *et al.* [14]. Figure 12 illustrates the temperature and streamfunction fields at a later time (denoted by the cross in figure 10). The simple unicellular flow has been replaced with an irregular convective pattern. We postulate that this irregular flow pattern is a result of the way in which our lateral symmetry boundary conditions constrain the system.

6 Conclusion

We have presented the results of a set of numerical experiments on a model of steady 2D unicellular convection in a fluid-saturated porous medium and quantified the heat transport over a range of Rayleigh numbers and aspect ratios. We observe that over the decade $Ra = 10^3$–10^4 the maximum value of the Nusselt number occurs in a cell whose aspect ratio scales as $L \sim Ra^{-1/2}$, and not as that of the fastest growing linear mode, i.e. $L \sim Ra^{-1/4}$, which may be postulated from the data presented in Otero *et al.* [14]. Furthermore, in this cell the heat transport is described by the scaling $Nu \sim Ra^{0.6}$.

Guided by our numerical results we have formulated an asymptotic reduction for the structure of the solutions that maximize the Nusselt number. We divide the cell into three subdomains: a central core region, and at both the top and bottom of the layer, a momentum boundary layer with a thinner thermal boundary layer within

it. With this reduction the heat transport is described by the scaling $Nu \sim Ra^{2/3}$. To complete the matched asymptotic analysis outlined here, the solutions in the boundary layers must be numerically computed and matched between the layers.

Our heat transport results from both the steady state numerical solutions and the matched asymptotic analysis differ from those given by the DNS of Otero *et al.* [14] and the classical scaling of Howard [10]. Graham & Steen [7] show that this scaling corresponds to the onset of plume formation; until then the appropriate scaling is $Nu \sim Ra^{2/3}$. However, plume formation is a time-dependent process, and therefore is not realisable in our steady model.

Furthermore, both the DNS and upper bound theory suggest that convection cells *within* the thermal boundary layer are required to achieve the $Nu \sim Ra$ scaling (Chini *et al.* [4]). Evidence of this can also be seen when we use our steady solution as the initial condition in a time-dependent model. In this case, at high Ra, Nu periodically approaches values reported by Otero *et al.* [14] and, in fact, appears to achieve the scaling $Nu \sim Ra^{0.92}$. At these times, embryonic rolls in the thermal boundary layer can be seen. However, the overall behaviour of the temperature and streamfunction fields in this time-dependent model is highly irregular, possibly as a result of the imposed lateral symmetry boundary conditions.

It remains to complete the asymptotic analysis, and to repeat the time-dependent numerical simulations with periodic lateral boundary conditions to see whether Nusselt numbers found by Otero *et al.* [14] are attained more consistently. In addition, it would be interesting to investigate whether a *multicellular* asymptotic structure, supporting convection cells within the thermal boundary layer and achieving the maximal Nu–Ra scaling, can be found.

Acknowledgements

References

[1] P. J. BLENNERHASSETT AND A. P. BASSOM, *Nonlinear high-wavenumber Bénard convection*, IMA J. Appl. Math., 52 (1994), pp. 51–77.

[2] J. P. BOYD, *Chebyshev and Fourier Spectral Methods*, Dover, 2nd ed., 2000.

[3] A. S. M. CHERKAOUI AND W. S. D. WILCOCK, *Characteristics of high Rayleigh number two-dimensional convection in an open-top porous layer heated from below*, J. Fluid Mech., 394 (1999), pp. 241–260.

[4] G. P. CHINI, N. DIANATI, Z. ZHANG, AND C. R. DOERING, *Low-dimensional models from upper bound theory*, Physica D, 240 (2011), pp. 241–248.

[5] C. R. DOERING AND P. CONSTANTIN, *Bounds for heat transport in a porous layer*, J. Fluid Mech., 376 (1998), pp. 263–296.

[6] A. C. FOWLER, *Mathematical models in the applied sciences*, Cambridge University Press, 1997.

[7] M. D. GRAHAM AND P. H. STEEN, *Plume formation and resonant bifurcations in porous-media convection*, J. Fluid Mech., 272 (1994), pp. 67–89.

[8] R. N. HORNE AND M. J. O'SULLIVAN, *Origin of oscillatory convection in a porous medium heated from below*, Phys. Fluids, 21 (1978), pp. 1260–1264.

[9] C. W. HORTON AND F. T. ROGERS, *Convection currents in a porous medium*, J. Appl. Phys., 16 (1945), pp. 367–370.

[10] L. N. HOWARD, *Convection at high Rayleigh numbers*, in Applied Mechanics, Proc. 11th Congress of Applied Mathematics, H. Gortler, ed., 1964, pp. 1109–1115.

[11] E. R. LAPWOOD, *Convection of a fluid in a porous medium*, Proc. Camb. Phil. Soc., 44 (1948), pp. 508–521.

[12] C. LISTER, *An explanation for the multivalued heat transport found experimentally for convection in a porous medium*, J. Fluid Mech., 214 (1990), pp. 287–320.

[13] D. A. NIELD AND A. BEJAN, *Convection in Porous Media*, Springer, 3rd ed., 2006.

[14] J. OTERO, L. A. DONTCHEVA, H. JOHNSTON, R. A. WORTHING, A. KURGANOV, G. PETROVA, AND C. R. DOERING, *High-Rayleigh-number convection in a fluid-saturated porous layer*, J. Fluid Mech., 500 (2004), pp. 263–281.

[15] E. PALM, J. E. WEBER, AND O. KVERNVOLD, *On steady convection in a porous medium*, J. Fluid Mech., 54 (1972), pp. 153–161.

[16] O. M. PHILLIPS, *Flow and Reactions in Permeable Rocks*, Cambridge University Press, 1991.

[17] ———, *Geological Fluid Dynamics: sub-surface flow and reactions*, Cambridge University Press, 2009.

[18] J. L. Robinson and M. J. O'Sullivan, *A boundary-layer model of flow in a porous medium at high Rayleigh number*, J. Fluid Mech., 75 (1976), pp. 459–467.

[19] N. Rudraiah and T. Musuoka, *Asymptotic analysis of natural convection through horizontal porous layer*, Int. J. Engng. Sci., 20 (1982), pp. 27–39.